ACS APPLIED MATERIALS & INTERFACES

Research Article

www.acsami.org

Surface Functionalization with Copper Tetraaminophthalocyanine Enables Efficient Charge Transport in Indium Tin Oxide Nanocrystal Thin Films

Mahdi Samadi Khoshkhoo,[†] Santanu Maiti,[‡] Frank Schreiber,[‡,§] Thomas Chassé,[†,§] and Marcus Scheele*[,†,§]

[†]Institute of Physical and Theoretical Chemistry, [‡]Institute of Applied Physics, and [§]Center for Light-Matter Interaction, Sensors & Analytics LISA+, University of Tübingen, 72076 Tübingen, Germany

Supporting Information

ABSTRACT: Macroscopic superlattices of tin-doped indium oxide (ITO) nanocrystals (NCs) are prepared by self-assembly at the air/liquid interface followed by simultaneous ligand exchange with the organic semiconductor copper 4,4′,4″,4‴-tetraaminophthalocyanine (Cu4APc). By using X-ray photoelectron spectroscopy (XPS), grazing-incidence small-angle X-ray scattering (GISAXS), and ultraviolet−visible−near-infrared (UV−vis−NIR) spectroscopy, we demonstrate that the semiconductor molecules largely replace the native surfactant from the ITO NC surface and act as cross-linkers between neighboring particles. Transport measurements reveal an increase in electrical conductance by 9 orders of magnitude, suggesting that Cu4APc provides efficient electronic coupling for neighboring ITO NCs. This material provides the opportunity to study charge and spin transport through phthalocyanine monolayers.

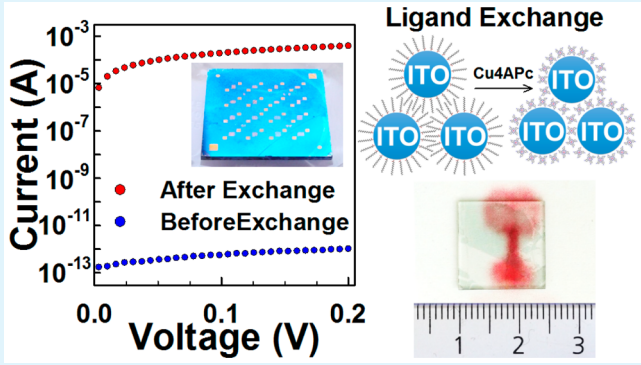

KEYWORDS: *colloidal nanocrystals, self-assembly, thin films, molecular electronics, nanoparticles, indium tin oxide (ITO), transparent electrodes, phthalocyanine*

1. INTRODUCTION

Exploiting the optoelectronic behavior of molecular monolayers or individual molecules sandwiched in between two electrodes bears exciting opportunities for nanoscale electronic devices.[1,2] Such "molecular electronics" is considered a promising means to continue the increasing miniaturization of memory chips as the length scale of current transistors is approaching the size of individual molecules.[3,4] The physics of molecular electronics is typically characterized by different transport mechanisms compared to conventional bulk crystalline conductors which holds for new possibilities to e.g. tune electronic coupling and design novel thermoelectric materials and sensors.[5−10] In order to study these effects, a key question to address is the choice of the contacts for the molecular junction.[11−13] One possibility in this respect is metal colloidal nanocrystals which are relatively cheap to synthesize, solution-processable, and tunable in shape.[14−18] Of particular advantage for molecular optoelectronics are (doped) metal oxide nanocrystals, which combine high optical transparencies in the visible regime with metallic electric conduction.[19−23] Such transparent electrodes are crucial in the design of single-molecular devices for photoswitching and light-emitting diodes, which are currently two very promising target applications of molecular electronics.[24,25]

In this work, we replace the native surfactant of tin-doped indium oxide (ITO) nanocrystals after synthesis by the organic semiconductor copper 4,4′,4″,4‴-tetraaminophthalocyanine (Cu4APc) to fabricate conductive and optically transparent thin films of ITO nanocrystals cross-linked with monolayers of Cu4APc. While previous studies typically applied thermal annealing to replace the surfactant from the surface of the metal oxide nanocrystals and/or induce particle sintering, a deliberate functionalization of these nanocrystals with conductive molecules has not been demonstrated to the best of our knowledge.[26−31] Metal phthalocyanines with nonzero spin are actively pursued as molecular magnets for single-molecule spintronics.[32−35] As recently suggested, the spin state of copper phthalocyanine molecules can potentially be manipulated by an external optical stimulus, holding for a promising combination of molecular optoelectronics with spintronics.[36] While the single molecule deposition of unsubstituted phthalocyanines is challenging due to their limited solubility, Cu4APc is easily soluble in common organic solvents. We show here that this allows synthesizing a hybrid material consisting of a network of

Received: January 12, 2017
Accepted: April 11, 2017
Published: April 11, 2017

DOI: 10.1021/acsami.7b00555
ACS Appl. Mater. Interfaces 2017, 9, 14197−14206

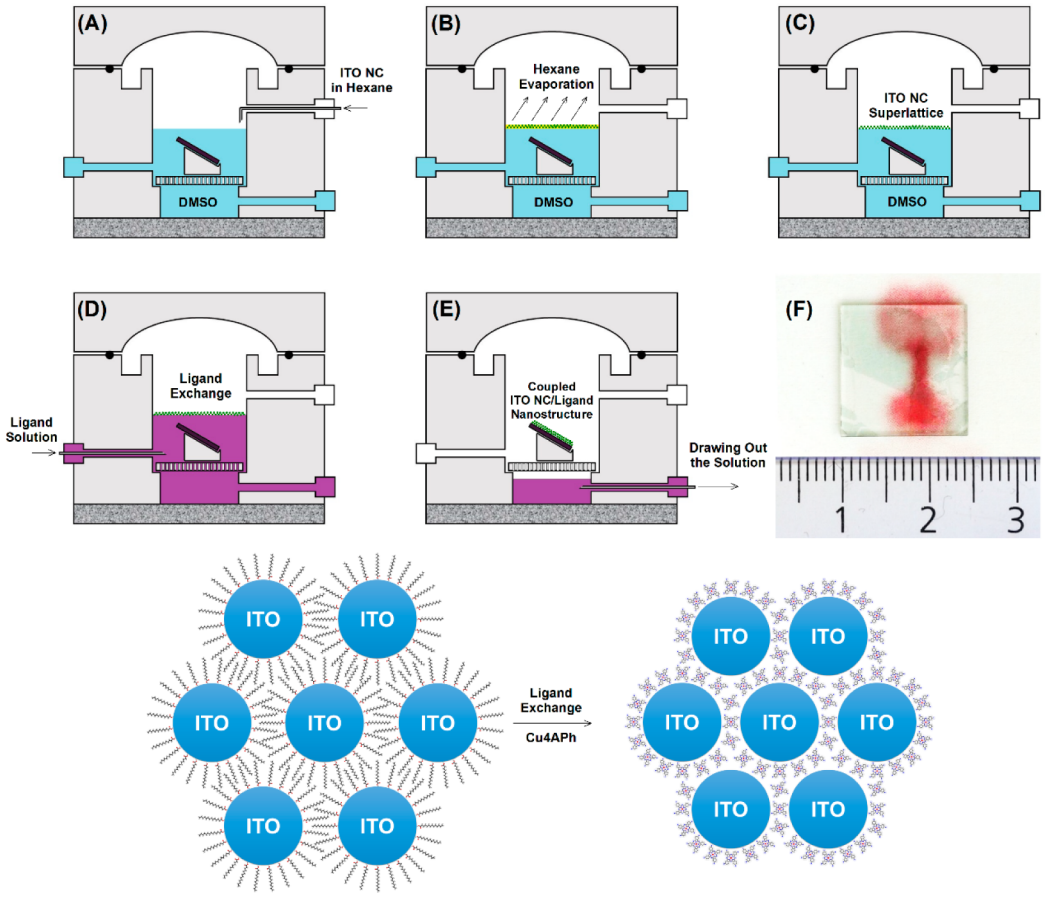

Figure 1. Fabrication process of electronically coupled large-area NC superlattice films. (A) The desired substrate is placed at the bottom of the chamber, and the chamber is filled with DMSO. A controlled amount of MA-capped ITO NCs dispersed in hexane is introduced to the DMSO surface. (B, C) An ultrathin film of NCs is formed upon spreading the NC dispersion on the liquid subphase and evaporation of hexane. (D) A solution of Cu4APc in DMSO is injected into the subphase to start the in-situ ligand exchange process. (E) The free-floating ligand-exchanged NC superlattice is transferred to the substrate by retracting the solution from the bottom of the chamber. (F) Photograph of the macroscopic, transparent, crack-free film of ITO NC/Cu4APc superlattice on a glass substrate.

isolated ITO nanocrystals, which are electronically connected by the molecular conductor.

2. METHODS

Synthesis of ITO Nanocrystals. ITO NCs were synthesized based on a previously reported method.[21] Briefly, an octadecene (20 mL of ODE) solution of indium and tin acetate (0.95 mmol of $In(Ac)_3$ and 0.05 mmol of $Sn(Ac)_2$) with myristic acid (3 mmol of MA) was degassed at 120 °C for 2 h in a three-neck flask attached to a Schlenk line. A similar preparation was performed with an ODE (10 mL) solution of octadecylamine (3 mmol of ODA). The carboxylic solution was heated to 295 °C under nitrogen in order to yield carboxylate precursors. Particle nucleation was initiated by rapid injection of the amine solution. The solution temperature was dropped to 280 °C and was maintained for 1 h. The solution color gradually changed from yellow to dark green within 5 min after injection. Afterward, the temperature was further reduced to 240 °C for 1 h. The NCs were collected by polarity-mediated precipitation using ethanol/chloroform, utilizing a high-speed centrifuge. Finally, the NCs were dispersed in *n*-hexane.

Synthesis of Copper 4,4′,4″,4‴-Tetraaminophthalocyanine (Cu4APc). Cu4APc was synthesized following a previously reported precedure.[37]

Self-Assembly of NC Superlattice and In-Situ Ligand Exchange at the Liquid–Air Interface. Electronically coupled large-area NC superlattice films were prepared by a Langmuir-type assembly at the liquid/air interface.[38−41] The fabrication process was carried out in a home-built Teflon chamber which is shown in Figure 1. In the first stage of the preparation, the desired substrate (TEM grid, amorphous glass, Au-patterned Si wafer for conductivity measurements, etc.) is placed at the bottom of the chamber, which is then filled with DMSO as a subphase liquid. 35 μL of MA-capped ITO NCs dispersed in hexane (with the concentration of approximately 1 mg/mL) is introduced to the DMSO surface (~200 μL/min) which after ~5 min leads to the self-assembly of a 1−2 monolayer thick film after evaporation of hexane (Figures 1A−C). In the second stage of the process, a solution of 0.25 mg/mL Cu4APc in DMSO is slowly injected into the subphase by a syringe in order to start the in-situ ligand exchange (Figure 1D). By adding the solution of Cu4APc to the subphase, simultaneous diffusion of phthalocyanine molecules into the NC superlattice and diffusion of primary organic ligand out of the floating film completes the ligand exchange process overnight. Finally, the free-floating ligand-exchanged NC superlattice is transferred to the substrate by retracting the solution from the bottom of the chamber and lowering the NC superlattice onto the solid substrate (Figure 1E).

Instrumentation. Particle size and shape were verified by scanning transmission electron microscopy (STEM) on a Hitachi SU 8030 microscope operating at 30 kV. The crystallographic phase of ITO was determined by X-ray diffraction (XRD) with an XRD-7000 X-ray diffractometer, Shimadzu Co., Japan, and Cu Kα radiation with λ = 1.5405 Å. In order to evaluate the dopant incorporation and surface characteristics, XPS measurements were carried out using a photoelectron spectrometer which was equipped with a conventional XR50 X-ray source (Al Kα, working at 12.5 kV and 20 mA, 1486.61 eV) and a PHOIBOS 100 MCD analyzer (SPECS). The pressure in the analyzer chamber was maintained below 3 × 10^{-10} mbar during the

DOI: 10.1021/acsami.7b00555
ACS Appl. Mater. Interfaces 2017, 9, 14197−14206

measurements. No changes in the core level signals of the as-prepared films and the films under X-ray irradiation were observed that represent the stability of the molecules during the data acquisition time. The resolution in XPS measurements was determined as 0.8 eV (calculated from the width of the Fermi edge on the Au substrate). The binding energies were corrected for electrical charge effects by referencing to Au 4f and adventitious C 1s peak, which were assumed to have a binding energy of 84.0 and 284.8 eV, respectively. The photoelectrons were detected at a takeoff angle of $\Phi = 0°$ with respect to the surface normal (normal emission). Each spectrum was corrected for the satellite peaks (Δ = 9.8 and 11.8 eV from Al Kα_3 and Al Kα_4, respectively). Data fitting was performed using Gauss–Lorentz profiles.[42] The background was calculated using the Shirley method. The relative tin content was determined by the ratio of the Sn 3d peak area to the total area of the In and Sn 3d peaks, scaled by the relative photoionization cross section for each element. The error introduced by differences in the escape depth of photoemitted electrons is neglected, since the binding energies of $3d_{5/2}$ signals for both In and Sn are close to each other. GISAXS measurements were performed at a laboratory-based Xeuss 2.0 instrument from Xenocs, France, with a wavelength of 1.5405 Å (Cu Kα). An incident beam of size 0.5 × 0.5 ($V \times H$) mm^2 was used with a grazing angle of 0.2° onto the surface of the sample. A two-dimensional Pilatus 300K detector was employed at a distance of 2.5 m from the sample center to collect the scattering spectra at low momentum transfer vector (q) value—to resolve the NPs size. Each sample was measured for 1 h to achieve good statistics. Optical measurements were performed on solid state films on glass substrates as well as dilute dispersions in tetrachloroethylene using an UV–vis–NIR spectrometer (Agilent Technologies, Cary 5000). The electrical measurements on the 2D NC array were performed using a Keithley 2634B dual source-meter unit, controlled by the included test script builder program. The free-floating ligand-exchanged NC superlattices were deposited on a commercially available bottom-gate, bottom-contact transistor substrates (Fraunhofer Institute for Photonic Microsystems, Dresden, Germany) with interdigitated Au electrodes of 10 mm width and varying channel lengths (2.5, 5, 10, and 20 μm; see Figure S3) followed by annealing at 250 °C for 2 h under a nitrogen atmosphere for further drying and improving the electrical conductance. Substrates were contacted using a home-built probe station enclosed in a nitrogen glovebox.

3. RESULTS

Figure 2A shows STEM images of a 1–2 monolayer thick film of MA-capped ITO NCs self-assembled into 2D close-packed arrays at the air/liquid interface recorded on a TEM grid. In contrast to other approaches,[40,43] the interface method yields 1–2 monolayer thick, large-area, free of crack interlinked nanoparticle arrays which can be easily transferred to the desired substrate. High-magnification STEM (Figure S1B) reveals that the NCs are well separated from each other by the myristic acid chains. The average particle size is found to be 6.8 nm by evaluating several STEM pictures from the same grid and counting more than 500 particles. The standard deviation with respect to the size is evaluated to be ~15%. The histogram for size analysis can be found in the Supporting Information (Figure S2). Figure 2B displays the XRD patterns for ITO NC films before and after annealing at 250 °C. First, the highly crystalline nature of the synthesized NCs is confirmed. The obtained patterns match very well with those of the standard cubic bixbyite phase of In_2O_3 (JCPDS no. 06-0416) and are in good agreement with those reported for ITO NCs in the literature.[21,22,44] Next, the X-ray diffraction pattern and peak widths remain unchanged after annealing, which provides supporting evidence that the crystal size remains fixed and the NCs do not fuse upon annealing.

XPS provides valuable information about compositional changes in the near-surface region. Figure 3 shows the XPS

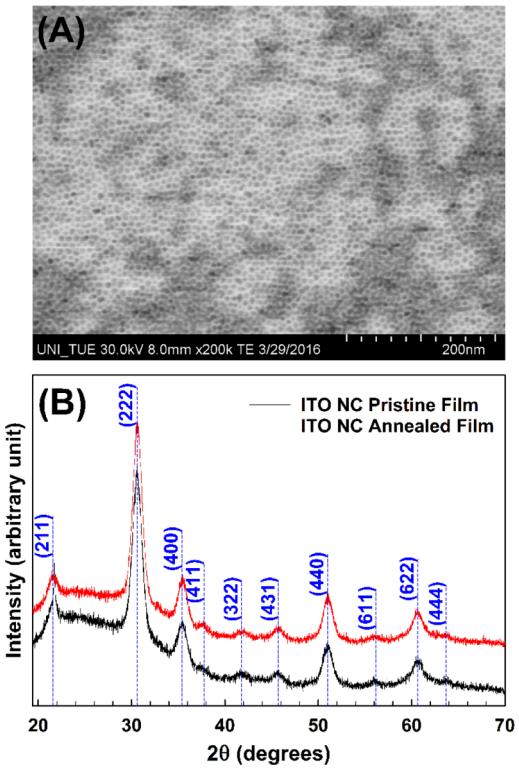

Figure 2. (A) Electron microscopy images of 1–2 monolayer thick film of myristic acid-capped ITO NC prepared at an air/liquid interface. (B) XRD patterns of ITO NC films before and after annealing.

spectra of the ITO NC superlattices prepared by the interface method before and after ligand exchange. As expected, one can detect indium, tin, oxygen, carbon (not shown here), and nitrogen. The latter element is only detected after ligand exchange. The individual core level spectra of O 1s, In 3d, Sn 3d, and N 1s are presented in parts A, B, C, and D of Figure 3, respectively. The O 1s core-level spectra could be fitted with four components of identical peak shape but various intensities labeled O_I (530.2 eV), O_{II} (531.5 eV), O_{III} (532.5 eV), and O_{IV} (533.5 eV) (see Figure 3A). After ligand exchange, the intensity of the O_{IV} component is significantly decreased and the $O_{III}/(O_I + O_{II})$ intensity ratio is considerably reduced. No change in the O_I/O_{II} intensity ratio is observed. The spin–orbit split In 3d and Sn 3d signals can be decomposed into two doublet peaks labeled In_I and In_{II} (In $3d_{5/2}$ component centered at 444.6 and 445.8 eV, respectively) and the peaks labeled Sn_I and Sn_{II} (Sn $3d_{5/2}$ component centered at 486.5 and 487.7 eV, respectively). No changes in their relative intensities are detected after ligand exchange (see Figures 3B,C). The relative tin content is calculated to be ~4.6% by taking the sensitivity factors of 13.32 and 14.8 for In $3d_{5/2}$ and Sn $3d_{5/2}$, respectively, using the ratio of the Sn 3d peak area to the total area of the In and Sn 3d signals. The observed line widths and positions of the main components of the In $3d_{5/2}$ (BE 444.6 eV) and Sn $3d_{5/2}$ (BE 486.5 eV) are in good accordance with earlier reports on the In^{3+} and the Sn^{4+} oxidation state in ITO.[45,46] The second components centered at 445.8 eV for In $3d_{5/2}$ and 487.7 eV for Sn $3d_{5/2}$ are attributed to surface-bound hydroxide.[47] Figure 3D represents the N 1s core-level signal for the ITO NCs superlattice film before and after ligand exchange. Before ligand exchange, no nitrogen signal can be detected in the film,

DOI: 10.1021/acsami.7b00555
ACS Appl. Mater. Interfaces 2017, 9, 14197–14206

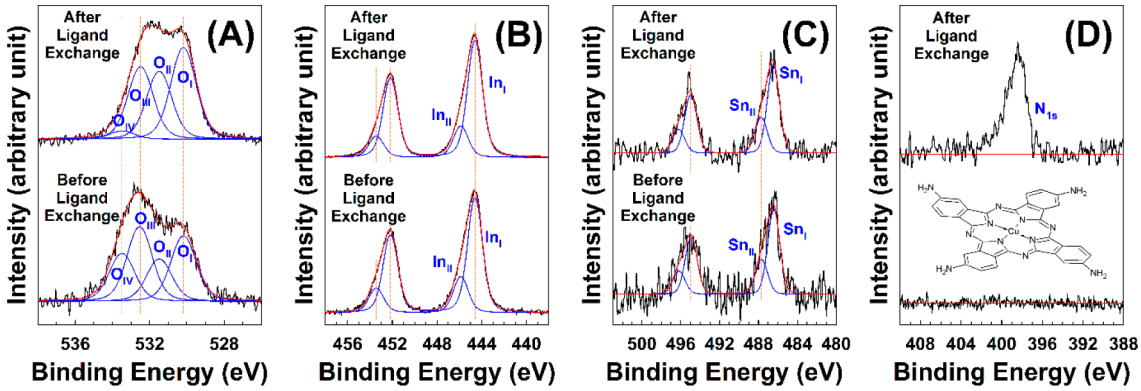

Figure 3. Core level XPS spectra of (A) O 1s, (B) In 3d, (C) Sn 3d, and (D) N 1s region of the ITO NCs superlattice films prepared by the interface method before and after ligand exchange.

but a strong signal appears after the exchange process. The inset in Figure 3D shows the chemical structure of Cu4APc.

Grazing-incidence small-angle X-ray scattering (GISAXS) is a very powerful tool for characterizing in-plane density correlations (i.e., typical distances, etc.) of nanoscale objects at surfaces or in thin films.[48,49] The GISAXS technique is highly surface sensitive as the incidence angle of X-ray is chosen near the critical angle of the film material, thus leading to a limited penetration depth (typically down to a few nanometers, if pushed to the extreme) and therefore reducing the scattering contribution of the substrate. GISAXS can provide information such as in-plane structural correlations or ordering among the assembled objects embedded in thin films and sizes of nano-objects including nanoparticles and islands.[48−52] This technique is used here to probe the ITO NC correlations in the prepared film of hybrid NCs-organic molecule network and to study the effect of ligand exchange and thermal annealing onto the self-assembled hybrid structure. For self-assembled monolayer films, the GISAXS patterns used to have largely vertical rods spectra whose position along q_y direction indicates the in-plane periodicity between the NCs, whereas the width of these reflections represents the degree of ordering among the NCs in the film. For MA-capped ITO NCs, we find an in-plane correlation "arc-like rod" scattering spectra at q_y = 0.0715 Å, which corresponds to the in-plane radial average distance of 8.8 nm between the NCs. We attribute the "arc-like rod" shape of the GISAXS signal to the presence few bi(multi)layer/buckled islands on top of a self-assembled hybrid monolayer of NCs and MA.[52] We note that while the relatively broad scattering patterns and the rather broad size distribution of the ITO NCs make conclusions on the exact absolute distances difficult, the relative changes upon sample annealing and ligand exchange as discussed in the following should be considered reliable. After thermal annealing of the same film at 250 °C for 2 h, the overall intensity of the GISAXS pattern is reduced by a factor of 1.4 (Figure 4B), possibly due to coalescence of some of the nanoparticles. More importantly, the in-plane correlation peak shifts toward higher q_y, corresponding to a decrease of the interparticle spacing along the in-plane direction by ∼0.6 nm. We attribute this contraction to the partial removal of MA. This also supported by the decreased scattering intensity, indicating a partial destruction of the superlattice or reduction of domain sizes. The GISAXS pattern of ITO NCs from the same batch after ligand exchange with Cu4APc is depicted in Figure 4C. The first-order correlation peak is found at q_y = 0.0785 Å^{-1}, corresponding to an average in-plane correlation distance between the nanoparticles of about 8.0 nm. In contrast to the MA-capped NCs, this distance is observed for the sample before annealing, such that it cannot be explained with thermal desorption or possible particle fusion. We attribute this to the significantly smaller size of Cu4APc (∼1.1 nm), acting as a cross-linker between adjacent NCs and establishing the ligand exchange process. We note that there is no further shift along q_y upon annealing the exchanged film at 250 °C for 2 h other than a reduction in scattering intensity (Figure 4D). The absence of significant changes in real-space correlation distances may be due the very strong interaction between ITO NCs and Cu4APc ligands and also the high melting point of the Cu4APc ligand itself.

Figure 5A displays the UV−vis−NIR absorption spectra of as-prepared ITO NC films before and after ligand exchange (red and black curves, respectively) as well as a dilute dispersion of MA-capped ITO NCs in tetrachloroethylene (blue curve). All samples show the interband transition of ITO at around 400 nm and a strong localized surface plasmon resonance (LSPR) peak in the near-infrared region indicating a significant density of free electrons. The position of the LSPR peak is red-shifted from 1740 nm for ITO NCs in dilute dispersion to 1984 nm for ITO NCs in thin films. These values are in good agreement with those reported in the literature.[22,53] After ligand exchange with Cu4APc, we observe the appearance of a new absorption band at 736 nm which is assigned to Cu4APc. In addition, the LSPR peak is further red-shifted from 1984 to 2016 nm. Figure 5B shows the UV−vis−NIR spectra of the same two films (MA- or Cu4APC-capping) after annealing at 250 °C for 2 h under a nitrogen atmosphere. Neglecting the small change in the shape of the Cu4APc feature, the maximum remains at 736 nm. In contrast, the LSPR peaks are significantly red-shifted to 2103 nm, but the effect is the same for both films.

In order to compare the electrical properties of the ITO NC films before and after ligand exchange, we extract the sheet resistance by low-field two-point current−voltage (I−V) measurements on substrates with prepatterned Au contacts in Figure 6. The sheet resistance is obtained from $R_s = Rw/l$, where R is the measured resistance of the 2D NC arrays, with L and w the length and width of the channel between two gold electrodes (2.5 μm and 10 mm, respectively). For the MA-capped ITO NCs, we find $R_s = 3.72 \times 10^{15}$ Ω/□ (blue circles) for films prepared at room temperature and $R_s = 2.45 \times 10^{13}$ Ω/□ (dark-blue circles) after annealing. Ligand exchange with Cu4APc reduces the sheet resistance to 5.97×10^{7} Ω/□ for films prepared at room temperature. Annealing further reduces

DOI: 10.1021/acsami.7b00555
ACS Appl. Mater. Interfaces 2017, 9, 14197−14206

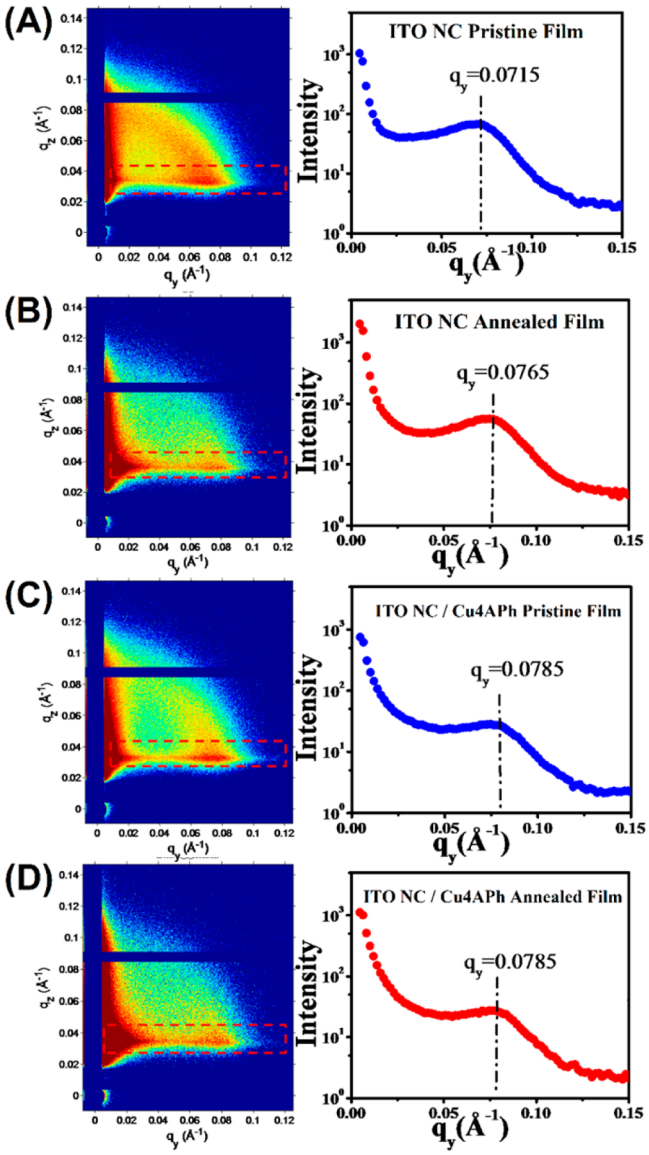

Figure 4. GISAXS of self-assembled ITO NCs arrays (A) capped with MA, (B) capped with MA and annealed at 250 °C for 2 h, (C) after ligand exchange with Cu4APc, and (D) after ligand exchange with Cu4APc and annealed at 250 °C for 2 h. Right panels: the extracted line profiles from the corresponding GISAXS images as a function of in-plane scattering vector q_y. To improve the statistics of the line profiles, the ROI (red dotted box) was integrated along the q_z direction. The footprint of the incident beam is 0.5 mm × 100 mm.

R_s by more than 1 order of magnitude (dark-red circles, 1.94 × 10^6 Ω/□). Thus, a dramatic increase in conductivity of the films by more than 9 orders of magnitude is observed after ligand exchange and annealing. A photograph of ITO NC films after exchange with Cu4APc on a prepatterned substrate for conductivity measurements is shown in the inset of Figure 6. In order to evaluate the contact resistance, we measure the total resistance for varying contact distances (see Figure S3) and apply the transmission line method (TLM).[54,55] The *y*-intercept of the fitted line gives the contact resistance and the slop multiply by *w* yields the sheet resistance. The extracted contact resistance is at least 2 orders of magnitude lower than the measured total resistance, indicating that its effect on our system is negligible.

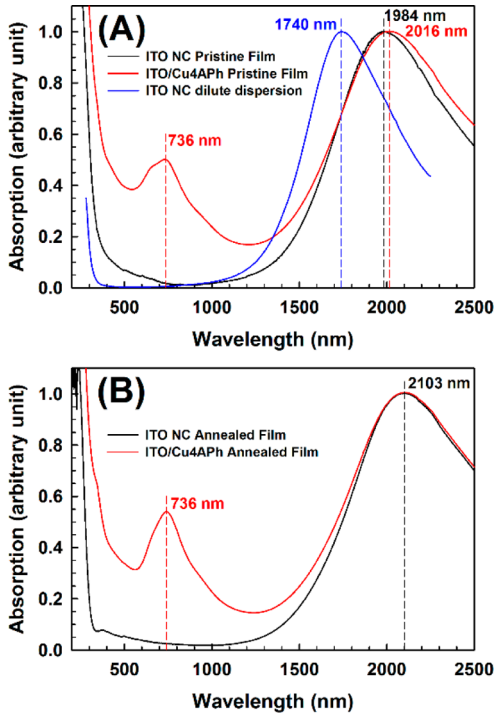

Figure 5. (A) UV−vis−NIR absorption spectra of ITO NC thin films before and after ligand exchange with Cu4PAc (red and black curves, respectively) as well as a dilute dispersion of ITO NCs in tetrachloroethylene (blue curve). (B) UV−vis−NIR absorption spectra of the same films after annealing at 250 °C for 2 h under a nitrogen atmosphere.

4. DISCUSSION

In this section, we first utilize the XPS data in Figure 3 to develop a chemical understanding of the ITO NC surface before and after ligand exchange with Cu4APc. We continue with analyzing the changes in optical (Figure 5) and electrical properties (Figure 6) upon ligand exchange with respect to the changes in the dielectric environment as well as structural changes elucidated by GISAXS in Figure 4. Finally, we comment on the transport properties of ITO-Cu4APc networks in the light of other reports on the electrical properties of metallic NCs.

Chemical Nature of the ITO NC Surface before and after Ligand Exchange. To elucidate the reactions involved in the ligand exchange from MA to Cu4APc at the ITO NC surface, we use our XPS results and previously reported XPS studies on macroscopic ITO samples to propose a possible scheme.[45−47,56−58] With respect to the four different oxygen species found in Figure 3 (O_I to O_{IV}), we make the following assignments: (O_I, BE 530.2 eV) O^{2-} ions bound to In^{3+} atoms; (O_{II}, BE 531.5 eV) O^{2-} ions next to vacancies in the In_2O_3 lattice;[46,47,58,59] (O_{III}, BE 532.5 eV) oxygen atoms in hydroxyl groups;[47,58] and (O_{IV}, BE 533.5 eV) carboxylic oxygen as part of the CO_2^- groups in MA and/or adventitious contaminations.[60] It is well-known that MA readily chemisorbs to ITO surfaces via its carboxylic acid headgroup, for instance by protonating the bridging oxides and hydroxyl groups or bounding to oxygen vacancies.[56] Figure 7 shows schematic views of the possible ITO NC surface before ligand exchange (part A) and the more complex surface after ligand exchange (part B). As the film fabrication and the ligand exchange processes are both carried out in direct exposure to ambient air

DOI: 10.1021/acsami.7b00555
ACS Appl. Mater. Interfaces 2017, 9, 14197−14206

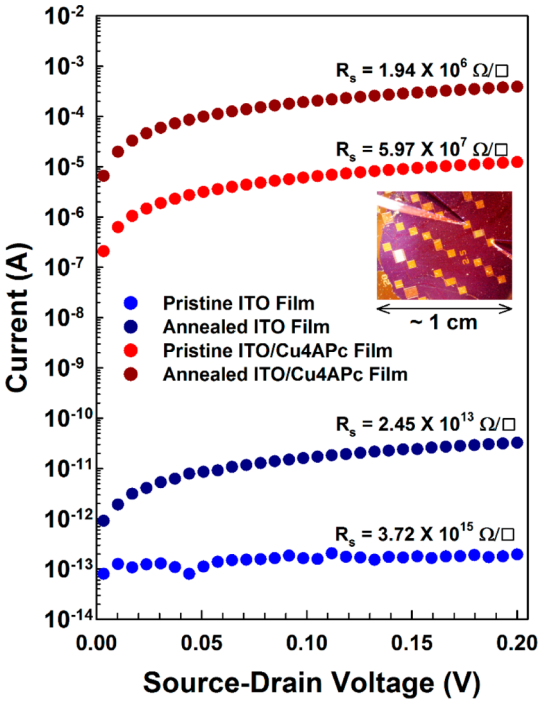

Figure 6. Current−voltage (I−V) characteristics as well as the sheet resistance measured for different processing histories of ITO NC films. Blue circles: MA-capped ITO NC films; dark-blue circles: MA-capped ITO NC films after annealing; red circles: ITO NC films after ligand exchange with Cu4APc; dark-red circles: ITO NC films after ligand exchange and annealing. The graph is plotted on a logarithmic scale for better comparison. Inset: photograph of a typical ITO NC film after exchange with Cu4APc on a prepatterned substrate with Au contacts for I−V measurements.

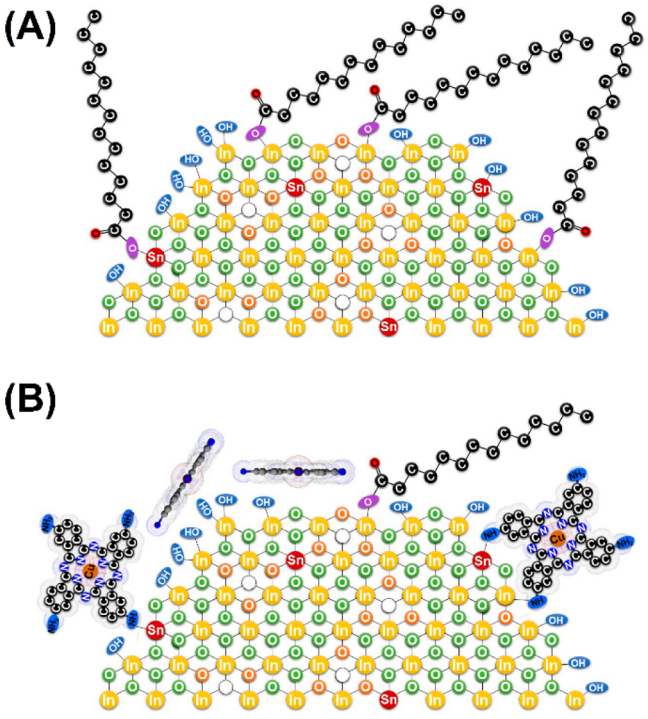

Figure 7. Schematic views of (A) the possible ITO NC surface before ligand exchange and (B) binding of the new incoming ligand molecules and the more complex surface after ligand exchange.

out of the glovebox, the residual water vapor can react with bridging oxygen atoms and also oxygen vacancy sites at the surface to form hydroxyl groups (Figure 7A).[57,58] After ligand exchange, the intensity of the O_{IV} signal is significantly decreased, suggesting that most of the MA molecules have been replaced from the ITO NC surface. Simultaneously, the new N 1s core-level signal confirms the presence of a nitrogen-rich species, such as Cu4APc (Figure 3D), in agreement with UV−vis−NIR results. This replacement is facilitated by the rather moderate binding strength of fatty acids to ITO.[47]

With respect to the preferred binding site of Cu4APc at the ITO surface, we suggest a reaction of the primary amino groups of the phthalocyanine and the NC surface hydroxyl groups according to

$$\mathrm{CuPh(NH_2)_4} + \mathrm{(ITO\ NC)M^+OH^-} \rightarrow \mathrm{(NH_2)_3CuPh(NH)-M(ITO\ NC)} + \mathrm{H_2O}$$

where M is the metal atom (In or Sn) at the surface. This is corroborated by our XPS results (Figure 3A), which indicate a substantial reduction of the $O_{III}/(O_I + O_{II})$ intensity ratio upon ligand exchange, that is, a loss of OH groups. It is worth pointing out that Cu4APc might also bind "side-on" to the ITO surface via its metal center atom (Figure 7B). Although we detected a very weak signal from the metal center of Cu4APc (Cu 2p, data not shown), due to the low concentration of copper atoms (only one atom per ligand molecule) and strong attenuation of this signal by the surrounding atoms the signal strength is too small to derive any meaningful information on the chemical environment of the Cu atom.

Correlation between Structure, Dielectric Environment, and Optoelectronic Properties. In good accordance with XPS, our GISAXS results also confirm the successful ligand exchange. In the as-prepared NC films, the nanoparticles are separated by MA molecules. The average correlation distance between neighboring NCs (center-to-center distance) is reduced by about 0.8 nm upon ligand exchange (Figure 4A vs 4C). This in the interparticle correlation distances matches with the difference between the molecular lengths of MA (~1.8 nm) and Cu4APc (~1.1 nm).

Decreasing the distance between two metallic NCs typically induces a red-shift of the LSPR due to a growing interaction of the surface electrons of the two NCs. In addition, changes in the dielectric environment of the surface electrons can also alter the LSPR.[61] We therefore attribute the 88 meV bathochromic shift of the LSPR for MA-capped ITO NCs obtained upon drying the NC solution on a substrate (Figure 5) to a mixture of these two effects, as the dielectric medium and the interparticle distance both change drastically in the process. In contrast, annealing of the dried ensemble primarily leads to a decrease in interparticle spacing, such that the additional 35 meV bathochromic shift of the LSPR of the MA-capped ITO NCs upon annealing are mainly attributed to a structural effect (Δd_{SL} = −0.6 nm). A comparison of the LSPRs of the dried NCs before and after ligand exchange indicates that in this case the different dielectric environment provided by Cu4APc supposedly causes a hypsochromic shift which competes with the shift due to the change in structure (Δd_{SL} = −0.8 nm): although the volume contraction is even larger than in the first case, the observed bathochromic shift is only 10 meV. Annealing of this sample does not lead to further volume contractions (see Figure 4), but the LSPR experiences another bathochromic shift by 25 meV which, as one possibility, we

DOI: 10.1021/acsami.7b00555
ACS Appl. Mater. Interfaces 2017, 9, 14197−14206

Table 1. Comparison of Recently Published Electrical Conductivities for Nanocrystalline ITO Thin Films

ref	σ (S cm^{-1})	NC diam (nm)	processing history	film thickness (nm)	Sn-doping concn (%)	surfactant
this work	0.5	6.8	annealed at 250 °C for 2 h	1−2 ML	5	Cu4APc
ref 29	0.001	10.5	25 °C	350	7	butanoate
ref 27	20	16	annealed at 500 °C	1100	5	n.a.
ref 30	200	11	annealed under 5% H_2 at 300 °C for 6 h	146	10	none
ref 28	1.7	9.5	as deposited by spin-coating	200	5	oleylamine
ref 26	1.0	14.6	350 °C in air for 10 min	165	10	none

attribute to the evaporation of the nonvolatile solvent DMSO and the associated change in the dielectric environment. Thus, although the LSPRs of the two annealed samples are practically identical, this is likely to be a coincidence since the dielectric environments are quite different.

Charge transport in arrays of metallic NCs is typically described within the framework of granular metals.[62−66] For transport in the dielectric regime, the resistance (R) follows a temperature-activated behavior according to

$$R \sim \exp\left(\frac{e^2}{\varepsilon d}\frac{1}{T}\right)^{\alpha} \quad (1)$$

with the elemental charge (e), the effective dielectric constant of the material ε, the effective localization length d, and the material-/temperature-specific coefficient α. Therefore, the sheet resistance in ITO NC networks is expected to be correlated to both the dielectric environment (represented by ε) and the structure (represented by d). In addition, the effective correlation length depends on the tunneling probability between adjacent NCs, which is again a function of structure (via the width of the tunneling barrier) and the chemical environment (e.g., due to a surrounding matrix with a nonzero conductance[67]). Our results in Figure 6 suggest that all investigated samples are in the dielectric regime since even for the most conductive sample (after ligand exchange and annealing), the estimated conductivity is on the order of 0.5 S cm^{-1} (assuming an average film thickness of 1−2 NC monolayers). This is 2 orders of magnitude lower than the expected conductivity for a coherently coupled network of metallic NCs with diameter a = 6.8 nm according to[68]

$$\sigma_{\mathrm{Coher}} \approx \frac{e^2}{ha} \quad (2)$$

This observation is in line with our GISAXS results which suggest that even after annealing the NCs remain well-separated, presumably by a monolayer of MA or Cu4APc. The slight decrease in R_s upon annealing MA-capped ITO thin films can be understood in terms of a reduction of the tunneling barrier width (Δd_{SL} = −0.6 nm). However, because of the largely insulating nature of MA, the tunneling probability increases only slightly due to the very large tunneling barrier height. The importance of the electronic structure of the surfactant in this respect is immediately apparent upon comparing the R_s values for ITO NC films before and after ligand exchange: Although the structural properties of the annealed MA-capped sample and the pristine Cu4APc-functionalized material (Figures 4B,C) are quite similar, the difference in conductivity is 5−6 orders of magnitude. Such a large change cannot be explained with an alteration of the dielectric environment alone and points to a dramatically enhanced tunneling probability between adjacent NCs via the semiconductor molecule. In contrast, the additional reduction of R_s after annealing of the Cu4APc-capped sample is probably mostly due to removal of the nonvolatile solvent DMSO, which is mainly a dielectric effect. On the other hand, annealing could also lead to beneficial geometric relaxation of Cu4APc at the ITO surface. We note that we did not observe any changes in XPS signals of ITO NCs capped with Cu4APc after annealing.

Comparison of the Transport Properties of Cu4APc-Capped ITO NCs with Other Reports on ITO NC Thin Films. Despite the parameters discussed in the section above, transport in ITO NC networks also strongly depends on the size of the NCs, the doping concentration, the processing history/annealing temperature, and the film thickness.[27,30,69]

Table 1 summarizes some recent results from the literature in terms of these additional parameters and demonstrates the large influence of the surface functionalization on the efficiency of charge transport between ITO NCs. Removing the surface molecules by annealing at $T \geq 300$ °C and/or under reductive conditions can lead to transport approaching the quantum conductance limit.[68] Here, transport is merely inhibited by the charging energy associated with injecting a charge into the confined volume of the NC. In contrast, if the surface functionalization remains intact, transport is predominantly limited by tunneling through the molecular layer and not by the charging energy of the NC. A comparison of the conductivity and lattice spacings measured in this work (0.5 S cm^{-1}; 1.2 nm) with that on similar ITO NC layers capped with butanoate (0.001 S cm^{-1}; 0.4 nm) implies that Cu4APc does not merely act as a molecular spacer but rather as an electronic bridge which greatly facilitates transport between adjacent NCs. In this sense, the material in the present work could also be viewed as an array of ITO contacts, which serve to study transport through molecular layers of Cu4APc. In the same context, it is instructive to compare the Cu4APc-ITO system with the vast literature of noble metal NCs (e.g., Au, Ag) separated by molecular monolayers,[70−72] such as saturated alkanethiols. Although the carrier concentration in such real metal NCs is significantly larger than in degenerately doped ITO, typical conductivities for molecular lengths of 1.2 nm are on the order of 10^{-3} S cm^{-1}. If the molecular layer is a semiconducting polymer, such as thiolated oligo(phenylene ethylene) (OPE) with a molecular length of 2.1 nm, a conductivity on the order of 0.02 S cm^{-1} has been reported.[15,16] These comparisons strongly suggest that carrier migration through the ITO-Cu4Pc network is remarkably efficient.

5. CONCLUSION

We have demonstrated that *in situ* ligand exchange of ITO nanocrystals at the liquid−air interface with semiconducting copper tetraaminophthalocyanine yields an electronically coupled network of well-separated nanocrystals. UV−vis−NIR, GISAXS, and XPS results demonstrate the presence/binding of the semiconductor ligand between/to the ITO nanocrystals. Two-point probe conductivity measurements

DOI: 10.1021/acsami.7b00555
ACS Appl. Mater. Interfaces 2017, 9, 14197−14206

reveal a dramatic decrease in sheet resistance by more than 9 orders of magnitude after ligand exchange, suggesting that the phthalocyanine derivative acts as an electronic linker. The synthetic concept pursued in this work enables future testing of theoretical models for the description of transport through granular metal systems as well as investigations of the interplay between organic semiconductor molecules with plasmonic nanocrystals.

■ ASSOCIATED CONTENT

Supporting Information

The Supporting Information is available free of charge on the ACS Publications website at DOI: 10.1021/acsami.7b00555.

Scanning transmission electron microscopy images, histogram for size analysis of nanocrystals, and evaluation of contact resistance applying transmission line method (TLM) (PDF)

■ AUTHOR INFORMATION

Corresponding Author

*E-mail: marcus.scheele@uni.tuebingen.de (M.S.).

ORCID

Marcus Scheele: 0000-0002-2704-3591

Notes

The authors declare no competing financial interest.

■ ACKNOWLEDGMENTS

The authors thank Mrs. Nadler for SEM/STEM measurements, Dr. Liang for assistance with XRD experiments, and the DFG for support under Grants SCHE1905/4 and SCHR700/25.

■ REFERENCES

(1) Aradhya, S. V.; Venkataraman, L. Single-Molecule Junctions beyond Electronic Transport. *Nat. Nanotechnol.* **2013**, *8*, 399−410.

(2) Kuhn, H.; Mobius, D. Systems of Monomolecular Layers - Assembling and Physico-Chemical Behavior. *Angew. Chem., Int. Ed. Engl.* **1971**, *10*, 620−637.

(3) Xiang, D.; Wang, X. L.; Jia, C. C.; Lee, T.; Guo, X. F. Molecular-Scale Electronics: From Concept to Function. *Chem. Rev.* **2016**, *116*, 4318−4440.

(4) Lortscher, E. Wiring Molecules Into Circuits. *Nat. Nanotechnol.* **2013**, *8*, 381−384.

(5) Frisenda, R.; van der Zant, H. S. J. Transition from Strong to Weak Electronic Coupling in a Single-Molecule Junction. *Phys. Rev. Lett.* **2016**, *117*, 126804.

(6) Guo, X. F.; Whalley, A.; Klare, J. E.; Huang, L. M.; O'Brien, S.; Steigerwald, M.; Nuckolls, C. Single-Molecule Devices as Scaffolding for Multicomponent Nanostructure Assembly. *Nano Lett.* **2007**, *7*, 1119−1122.

(7) Malen, J. A.; Doak, P.; Baheti, K.; Tilley, T. D.; Segalman, R. A.; Majumdar, A. Identifying the Length Dependence of Orbital Alignment and Contact Coupling in Molecular Heterojunctions. *Nano Lett.* **2009**, *9*, 1164−1169.

(8) Reddy, P.; Jang, S. Y.; Segalman, R. A.; Majumdar, A. Thermoelectricity in Molecular Junctions. *Science* **2007**, *315*, 1568−1571.

(9) Rincon-Garcia, L.; Evangeli, C.; Rubio-Bollinger, G.; Agrait, N. Thermopower Measurements in Molecular Junctions. *Chem. Soc. Rev.* **2016**, *45*, 4285−4306.

(10) Schlicke, H.; Battista, D.; Kunze, S.; Schroter, C. J.; Eich, M.; Vossmeyer, T. Freestanding Membranes of Cross-Linked Gold Nanoparticles: Novel Functional Materials for Electrostatic Actuators. *ACS Appl. Mater. Interfaces* **2015**, *7*, 15123−15128.

(11) Dubois, V.; Niklaus, F.; Stemme, G. Crack-Defined Electronic Nanogaps. *Adv. Mater.* **2016**, *28*, 2178−2182.

(12) Requist, R.; Baruselli, P. P.; Smogunov, A.; Fabrizio, M.; Modesti, S.; Tosatti, E. Metallic, Magnetic and Molecular Nanocontacts. *Nat. Nanotechnol.* **2016**, *11*, 499−508.

(13) Su, T. A.; Neupane, M.; Steigerwald, M. L.; Venkataraman, L.; Nuckolls, C. Chemical Principles of Single-Molecule Electronics. *Nat. Rev. Mater.* **2016**, *1*, 16002.

(14) Bernard, L.; Kamdzhilov, Y.; Calame, M.; van der Molen, S. J.; Liao, J. H.; Schonenberger, C. Spectroscopy of Molecular Junction Networks Obtained by Place Exchange in 2D Nanoparticle Arrays. *J. Phys. Chem. C* **2007**, *111*, 18445−18450.

(15) Liao, J.; Bernard, L.; Langer, M.; Schonenberger, C.; Calame, M. Reversible Formation of Molecular Junctions in 2D Nanoparticle Arrays. *Adv. Mater.* **2006**, *18*, 2444−2447.

(16) Liao, J. H.; Blok, S.; van der Molen, S. J.; Diefenbach, S.; Holleitner, A. W.; Schonenberger, C.; Vladyka, A.; Calame, M. Ordered Nanoparticle Arrays Interconnected by Molecular Linkers: Electronic and Optoelectronic Properties. *Chem. Soc. Rev.* **2015**, *44*, 999−1014.

(17) Wessels, J. M.; Nothofer, H. G.; Ford, W. E.; von Wrochem, F.; Scholz, F.; Vossmeyer, T.; Schroedter, A.; Weller, H.; Yasuda, A. Optical and Electrical Properties of Three-Dimensional Interlinked Gold Nanoparticle Assemblies. *J. Am. Chem. Soc.* **2004**, *126*, 3349−3356.

(18) Xia, Y. N.; Xiong, Y. J.; Lim, B.; Skrabalak, S. E. Shape-Controlled Synthesis of Metal Nanocrystals: Simple Chemistry Meets Complex Physics? *Angew. Chem., Int. Ed.* **2009**, *48*, 60−103.

(19) Buonsanti, R.; Llordes, A.; Aloni, S.; Helms, B. A.; Milliron, D. J. Tunable Infrared Absorption and Visible Transparency of Colloidal Aluminum-Doped Zinc Oxide Nanocrystals. *Nano Lett.* **2011**, *11*, 4706−4710.

(20) Buonsanti, R.; Milliron, D. J. Chemistry of Doped Colloidal Nanocrystals. *Chem. Mater.* **2013**, *25*, 1305−1317.

(21) Gilstrap, R. A.; Capozzi, C. J.; Carson, C. G.; Gerhardt, R. A.; Summers, C. J. Synthesis of a Nonagglomerated Indium Tin Oxide Nanoparticle Dispersion. *Adv. Mater.* **2008**, *20*, 4163−4166.

(22) Kanehara, M.; Koike, H.; Yoshinaga, T.; Teranishi, T. Indium Tin Oxide Nanoparticles with Compositionally Tunable Surface Plasmon Resonance Frequencies in the Near-IR Region. *J. Am. Chem. Soc.* **2009**, *131*, 17736−17737.

(23) Llordes, A.; Garcia, G.; Gazquez, J.; Milliron, D. J. Tunable Near-Infrared and Visible-Light Transmittance in Nanocrystal-in-Glass Composites. *Nature* **2013**, *500*, 323−326.

(24) Reecht, G.; Scheurer, F.; Speisser, V.; Dappe, Y. J.; Mathevet, F.; Schull, G. Electroluminescence of a Polythiophene Molecular Wire Suspended between a Metallic Surface and the Tip of a Scanning Tunneling Microscope. *Phys. Rev. Lett.* **2014**, *112*, 047403.

(25) Dulic, D.; van der Molen, S. J.; Kudernac, T.; Jonkman, H. T.; de Jong, J. J. D.; Bowden, T. N.; van Esch, J.; Feringa, B. L.; van Wees, B. J. One-Way Optoelectronic Switching of Photochromic Molecules on Gold. *Phys. Rev. Lett.* **2003**, *91*, 207402.

(26) Diroll, B. T.; Gordon, T. R.; Gaulding, E. A.; Klein, D. R.; Paik, T.; Yun, H. J.; Goodwin, E. D.; Damodhar, D.; Kagan, C. R.; Murray, C. B. Synthesis of N-Type Plasmonic Oxide Nanocrystals and the Optical and Electrical Characterization of their Transparent Conducting Films. *Chem. Mater.* **2014**, *26*, 4579−4588.

(27) Ederth, J.; Johnsson, P.; Niklasson, G. A.; Hoel, A.; Hultaker, A.; Heszler, P.; Granqvist, C. G.; van Doorn, A. R.; Jongerius, M. J.; Burgard, D. Electrical and Optical Properties of Thin Films Consisting of Tin-Doped Indium Oxide Nanoparticles. *Phys. Rev. B: Condens. Matter Mater. Phys.* **2003**, *68*, 155410.

(28) Ephraim, J.; Lanigan, D.; Staller, C.; Milliron, D. J.; Thimsen, E. Transparent Conductive Oxide Nanocrystals Coated with Insulators by Atomic Layer Deposition. *Chem. Mater.* **2016**, *28*, 5549−5553.

(29) Grisolia, J.; Decorde, N.; Gauvin, M.; Sangeetha, N. M.; Viallet, B.; Ressier, L. Electron Transport within Transparent Assemblies of Tin-Doped Indium Oxide Colloidal Nanocrystals. *Nanotechnology* **2015**, *26*, 335702.

DOI: 10.1021/acsami.7b00555
ACS Appl. Mater. Interfaces 2017, 9, 14197−14206

(30) Lee, J.; Lee, S.; Li, G. L.; Petruska, M. A.; Paine, D. C.; Sun, S. H. A Facile Solution-Phase Approach to Transparent and Conducting ITO Nanocrystal Assemblies. *J. Am. Chem. Soc.* **2012**, *134*, 13410−13414.
(31) Shanker, G. S.; Tandon, B.; Shibata, T.; Chattopadhyay, S.; Nag, A. Doping Controls Plasmonics, Electrical Conductivity, and Carrier-Mediated Magnetic Coupling in Fe and Sn Codoped In2O3 Nanocrystals: Local Structure Is the Key. *Chem. Mater.* **2015**, *27*, 892−900.
(32) Hsu, C. H.; Chu, Y. H.; Lu, C. I.; Hsu, P. J.; Chen, S. W.; Hsueh, W. J.; Kaun, C. C.; Lin, M. T. Spin-Polarized Transport through Single Manganese Phthalocyanine Molecules on a Co Nanoisland. *J. Phys. Chem. C* **2015**, *119*, 3374−3378.
(33) Thiele, S.; Balestro, F.; Ballou, R.; Klyatskaya, S.; Ruben, M.; Wernsdorfer, W. Electrically Driven Nuclear Spin Resonance in Single-Molecule Magnets. *Science* **2014**, *344*, 1135−1138.
(34) Brede, J.; Atodiresei, N.; Kuck, S.; Lazic, P.; Caciuc, V.; Morikawa, Y.; Hoffmann, G.; Blugel, S.; Wiesendanger, R. Spin- and Energy-Dependent Tunneling through a Single Molecule with Intramolecular Spatial Resolution. *Phys. Rev. Lett.* **2010**, *105*, 047204.
(35) Bogani, L.; Wernsdorfer, W. Molecular Spintronics Using Single-Molecule Magnets. *Nat. Mater.* **2008**, *7*, 179−186.
(36) Wu, W. Exchange Interaction between the Triplet Exciton and the Localized Spin in Copper-Phthalocyanine. *J. Chem. Phys.* **2014**, *140*, 224301.
(37) Jung, S. H.; Choi, J. H.; Yang, S. M.; Cho, W. J.; Ha, C. S. Syntheses and Characterization of Soluble Phthalocyanine Derivatives for Organic Electroluminescent Devices. *Mater. Sci. Eng., B* **2001**, *85*, 160−164.
(38) Dong, A. G.; Chen, J.; Oh, S. J.; Koh, W. K.; Xiu, F. X.; Ye, X. C.; Ko, D. K.; Wang, K. L.; Kagan, C. R.; Murray, C. B. Multiscale Periodic Assembly of Striped Nanocrystal Super lattice Films on a Liquid Surface. *Nano Lett.* **2011**, *11*, 841−846.
(39) Dong, A. G.; Jiao, Y. C.; Milliron, D. J. Electronically Coupled Nanocrystal Superlattice Films by in Situ Ligand Exchange at the Liquid-Air Interface. *ACS Nano* **2013**, *7*, 10978−10984.
(40) Andre, A.; Zherebetskyy, D.; Hanifi, D.; He, B.; Khoshkhoo, M. S.; Jankowski, M.; Chasse, T.; Wang, L. W.; Schreiber, F.; Salleo, A.; Liu, Y.; Scheele, M. Toward Conductive Mesocrystalline Assemblies: PbS Nanocrystals Cross-Linked with Tetrathiafulvalene Dicarboxylate. *Chem. Mater.* **2015**, *27*, 8105−8115.
(41) Sharma, R.; Sawvel, A. M.; Barton, B.; Dong, A. G.; Buonsanti, R.; Llordes, A.; Schaible, E.; Axnanda, S.; Liu, Z.; Urban, J. J.; Nordlund, D.; Kisielowski, C.; Milliron, D. J. Nanocrystal Superlattice Embedded within an Inorganic Semiconducting Matrix by in Situ Ligand Exchange: Fabrication and Morphology. *Chem. Mater.* **2015**, *27*, 2755−2758.
(42) Hesse, R.; Chasse, T.; Szargan, R. Unifit 2002 - Universal Analysis Software for Photoelectron Spectra. *Anal. Bioanal. Chem.* **2003**, *375*, 856−863.
(43) Luther, J. M.; Law, M.; Song, Q.; Perkins, C. L.; Beard, M. C.; Nozik, A. J. Structural, Optical and Electrical Properties of Self-Assembled Films of PbSe Nanocrystals Treated with 1,2-Ethanedithiol. *ACS Nano* **2008**, *2*, 271−280.
(44) Choi, S. I.; Nam, K. M.; Park, B. K.; Seo, W. S.; Park, J. T. Preparation and Optical Properties of Colloidal, Monodisperse, and Highly Crystalline ITO Nanoparticles. *Chem. Mater.* **2008**, *20*, 2609−2611.
(45) Yan, C.; Zharnikov, M.; Golzhauser, A.; Grunze, M. Preparation and Characterization of Self-Assembled Monolayers on Indium Tin Oxide. *Langmuir* **2000**, *16*, 6208−6215.
(46) Kim, J. S.; Ho, P. K. H.; Thomas, D. S.; Friend, R. H.; Cacialli, F.; Bao, G. W.; Li, S. F. Y. X-ray Photoelectron Spectroscopy of Surface-Treated Indium-Tin Oxide Thin Films. *Chem. Phys. Lett.* **1999**, *315*, 307−312.
(47) Karsi, N.; Lang, P.; Chehimi, M.; Delamar, M.; Horowitz, G. Modification of Indium Tin Oxide Films by Alkanethiol and Fatty Acid Self-Assembled Monolayers: A Comparative Study. *Langmuir* **2006**, *22*, 3118−3124.
(48) Renaud, G.; Lazzari, R.; Leroy, F. Probing Surface and Interface Morphology with Grazing Incidence Small Angle X-Ray Scattering. *Surf. Sci. Rep.* **2009**, *64*, 255−380.
(49) Muller-Buschbaum, P. Grazing Incidence Small-Angle X-ray Scattering: an Advanced Scattering Technique for the Investigation of Nanostructured Polymer Films. *Anal. Bioanal. Chem.* **2003**, *376*, 3−10.
(50) Maiti, S.; Sanyal, M. K.; Jana, M. K.; Runge, B.; Murphy, B. M.; Biswas, K.; Rao, C. N. R. Evidence of Contact Epitaxy in the Self-Assembly of HgSe Nanocrystals Formed at a Liquid−Liquid Interface. *J. Phys.: Condens. Matter* **2017**, *29*, 095101.
(51) Frank, C.; Banerjee, R.; Oettel, M.; Gerlach, A.; Novak, J.; Santoro, G.; Schreiber, F. Analysis of Island Shape Evolution from Diffuse X-ray Scattering of Organic Thin Films and Implications for Growth. *Phys. Rev. B: Condens. Matter Mater. Phys.* **2014**, *90*, 205401.
(52) Bera, M. K.; Sanyal, M. K.; Pal, S.; Daillant, J.; Datta, A.; Kulkarni, G. U.; Luzet, D.; Konovalov, O. Reversible Buckling in Monolayer of Gold Nanoparticles on Water Surface. *EPL* **2007**, *78*, 56003.
(53) Garcia, G.; Buonsanti, R.; Runnerstrom, E. L.; Mendelsberg, R. J.; Llordes, A.; Anders, A.; Richardson, T. J.; Milliron, D. J. Dynamically Modulating the Surface Plasmon Resonance of Doped Semiconductor Nanocrystals. *Nano Lett.* **2011**, *11*, 4415−4420.
(54) Andre, A.; Theurer, C.; Lauth, J.; Maiti, S.; Hodas, M.; Samadi Khoshkhoo, M.; Kinge, S.; Meixner, A. J.; Schreiber, F.; Siebbeles, L. D. A.; Braun, K.; Scheele, M. Structure, Transport and Photoconductance of PbS Quantum Dot Monolayers Functionalized with a Copper Phthalocyanine Derivative. *Chem. Commun.* **2017**, *53*, 1700−1703.
(55) Zaumseil, J.; Baldwin, K. W.; Rogers, J. A. Contact Resistance in Organic Transistors that use Source and Drain Electrodes Formed by Soft Contact Lamination. *J. Appl. Phys.* **2003**, *93*, 6117−6124.
(56) Havare, A. K.; Can, M.; Demic, S.; Okur, S.; Kus, M.; Aydin, H.; Yagmurcukardes, N.; Tari, S. Modification of ITO Surface using Aromatic Small Molecules with Carboxylic Acid Groups for OLED Applications. *Synth. Met.* **2011**, *161*, 2397−2404.
(57) Brumbach, M.; Veneman, P. A.; Marrikar, F. S.; Schulmeyer, T.; Simmonds, A.; Xia, W.; Lee, P.; Armstrong, N. R. Surface Composition and Electrical and Electrochemical Properties of Freshly Deposited and Acid-Etched Indium Tin Oxide Electrodes. *Langmuir* **2007**, *23*, 11089−11099.
(58) Donley, C.; Dunphy, D.; Paine, D.; Carter, C.; Nebesny, K.; Lee, P.; Alloway, D.; Armstrong, N. R. Characterization of Indium-Tin Oxide Interfaces using X-ray Photoelectron Spectroscopy and Redox Processes of a Chemisorbed Probe Molecule: Effect of Surface Pretreatment Conditions. *Langmuir* **2002**, *18*, 450−457.
(59) Fan, J. C. C.; Goodenough, J. B. X-Ray Photoemission Spectroscopy Studies of Sn-Doped Indium-Oxide Films. *J. Appl. Phys.* **1977**, *48*, 3524−3531.
(60) López, G. P.; Castner, D. G.; Ratner, B. D. XPS O 1s Binding Energies for Polymers Containing Hydroxyl, Ether, Ketone and Ester groups. *Surf. Interface Anal.* **1991**, *17*, 267−272.
(61) Mie, G. Beiträge zur Optik Trüber Medien, Speziell Kolloidaler Metallösungen. *Ann. Phys.* **1908**, *330*, 377−445.
(62) Huth, M. Granular Metals: From Electronic Correlations to Strain-Sensing Applications. *J. Appl. Phys.* **2010**, *107*, 113709.
(63) Beloborodov, I. S.; Lopatin, A. V.; Vinokur, V. M.; Efetov, K. B. Granular Electronic Systems. *Rev. Mod. Phys.* **2007**, *79*, 469−518.
(64) Sheng, P. Electronic Transport in Granular Metal-Films. *Philos. Mag. B* **1992**, *65*, 357−384.
(65) Efros, A. L.; Shklovskii, B. I. Coulomb Gap and Low-Temperature Conductivity of Disordered Systems. *J. Phys. C: Solid State Phys.* **1975**, *8*, L49−L51.
(66) Sheng, P.; Abeles, B.; Arie, Y. Hopping Conductivity in Granular Metals. *Phys. Rev. Lett.* **1973**, *31*, 44−47.
(67) Zabet-Khosousi, A.; Trudeau, P. E.; Suganuma, Y.; Dhirani, A. A.; Statt, B. Metal to Insulator Transition in Films of Molecularly Linked Gold Nanoparticles. *Phys. Rev. Lett.* **2006**, *96*, 156403.
(68) Guyot-Sionnest, P. Electrical Transport in Colloidal Quantum Dot Films. *J. Phys. Chem. Lett.* **2012**, *3*, 1169−1175.

DOI: 10.1021/acsami.7b00555
ACS Appl. Mater. Interfaces 2017, 9, 14197−14206

(69) Yun, J.; Park, Y. H.; Bae, T. S.; Lee, S.; Lee, G. H. Fabrication of a Completely Transparent and Highly Flexible ITO Nanoparticle Electrode at Room Temperature. *ACS Appl. Mater. Interfaces* **2013**, *5*, 164−172.
(70) Zabet-Khosousi, A.; Dhirani, A. A. Charge Transport in Nanoparticle Assemblies. *Chem. Rev.* **2008**, *108*, 4072−4124.
(71) Love, J. C.; Estroff, L. A.; Kriebel, J. K.; Nuzzo, R. G.; Whitesides, G. M. Self-Assembled Monolayers of Thiolates on Metals as a Form of Nanotechnology. *Chem. Rev.* **2005**, *105*, 1103−1169.
(72) Schreiber, F. Structure and Growth of Self-Assembling Monolayers. *Prog. Surf. Sci.* **2000**, *65*, 151−256.

DOI: 10.1021/acsami.7b00555
ACS Appl. Mater. Interfaces 2017, 9, 14197−14206